Two-Dimensional Correlation Spectroscopy of Two-Exciton Resonances in Semiconductor Quantum Wells

Lijun Yang and Shaul Mukamel

Chemistry Department, University of California, Irvine, California 92697-2025, United States, USA

(Received 7 June 2007; published 4 February 2008)

We propose a three-pulse coherent ultrafast optical technique that is particularly sensitive to two-exciton correlations. Two Liouville-space pathways for the density matrix contribute to this signal which reveals double quantum coherences when displayed as a two-dimensional correlation plot. Two-exciton couplings spread the cross peaks along both axes, creating a characteristic highly resolved pattern. This level of detail is not available from conventional one-dimensional four-wave mixing or other two-dimensional correlation spectroscopy signals such as the photo echo, in which two-exciton couplings show up along a single axis and are highly congested.

DOI: 10.1103/PhysRevLett.100.057402 PACS numbers: 78.47.−p, 42.50.Md, 71.35.Cc, 78.67.De

Investigating the correlations of multiple excitons in semiconductors is a challenging many-body problem that had drawn considerable theoretical [1–5] and experimental [6,7] attention. Correlations of two excitons beyond the Hartree-Fock (HF) approximation may result in either a redshift [two-exciton binding energy (TBE)] or a blueshift [two-exciton scattering energy (TSE)]. In GaAs semiconductor quantum wells both couplings are a few meV s and may not be easily resolved. Two-exciton formation has been reviewed in Refs. [6,8]. Coherent ultrafast four-wave mixing (FWM) [6] provides a direct probe for two-exciton correlations in quantum wells. The best evidence for bound two excitons and the most accurate TBE in GaAs quantum wells are obtained by time integrated FWM (TIFWM), where signals are displayed as a function of a single (time or frequency) variable [6,9,10]. Quantum beats were observed in the negative-delay two-pulse signal along $2\mathbf{k}_b - \mathbf{k}_a$, where $\mathbf{k}_b$ arrives first, and in the positive-delay three-pulse signal along $\mathbf{k}_a + \mathbf{k}_b - \mathbf{k}_c$ ($\mathbf{k}_c$ comes after $\mathbf{k}_b$). Some attempts have been made to enhance the spectral resolution by displaying FWM signals versus two time variables [11,12].

Multidimensional analysis of coherent signals is commonly used in NMR to study correlations between spins [13]. These techniques were recently extended to the femtosecond regime [14] and applied to several chemical and biological systems [15,16]. Three ultrashort laser pulses generate a signal which is heterodyne detected by a fourth pulse in a chosen phase-matching direction (Fig. 1, top left). Three time delays (t_1, t_2, and t_3) can be controlled between the chronologically ordered pulses, $\mathbf{k}_1$, $\mathbf{k}_2$, and $\mathbf{k}_3$, and the heterodyne pulse $\mathbf{k}_s$. For an excitonic system the signal can be generated along the phase-matching directions, $-\mathbf{k}_1 + \mathbf{k}_2 + \mathbf{k}_3$, $\mathbf{k}_1 - \mathbf{k}_2 + \mathbf{k}_3$, and $\mathbf{k}_1 + \mathbf{k}_2 - \mathbf{k}_3$. We denote these three techniques as $S_{\mathbf{I}}$, $S_{\mathbf{II}}$, and $S_{\mathbf{III}}$ [14,17] respectively. The time-domain nonlinear response is given by combinations of multitime correlation functions which depend on the time delays t_1, t_2, and t_3. Displaying the signal as a function of two time delays (or their conjugate frequencies) while holding the third fixed gives the two-dimensional correlation spectroscopy (2DCS) signals. Note that t_1, t_2, and t_3 are positive. This is different from conventional FWM where there is no fixed time ordering among the $\mathbf{k}_a$, $\mathbf{k}_b$, and $\mathbf{k}_c$ pulses and their delays can be either positive or negative. We show that controlling the time ordering in 2DCS is critical for the unambiguous identification of many-body correlations. $S_{\mathbf{I}}$ (photon echo) signals were recently reported in GaAs heterostructures [18–21]. In this Letter, we demonstrate that the $S_{\mathbf{III}}$ technique, when displayed in a proper projection plane, can access electronic correlations beyond the HF approximation such as bound and unbound two excitons with very high resolution, not available in 1D FWM and any other 2DCS techniques.

We employ a multiband 1D tight-binding Hamiltonian [22,23] for calculating the $S_{\mathbf{III}}$ signal. It includes a simplified Coulomb interaction and accounts for the heavy-hole (HH) and light-hole excitons and their continuum

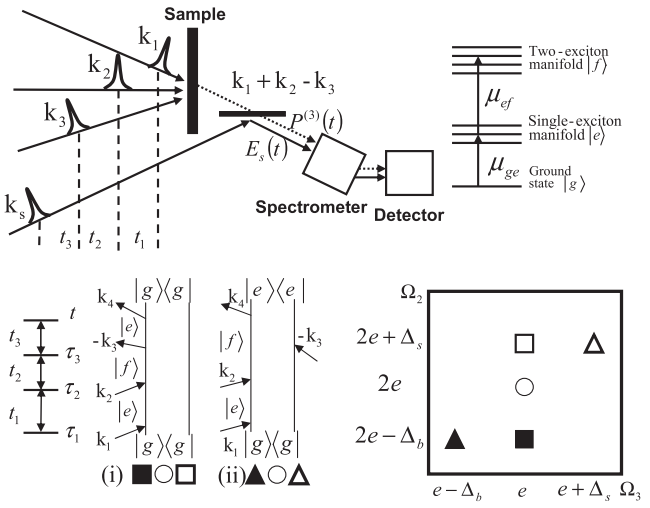

FIG. 1. Top: Schematic experimental setup (left) and exciton level scheme (right). Bottom: Feynman diagrams of the $S_{\mathbf{III}}$ technique (left) and the schematic 2D spectrum (right).

states in a tractable way. This model successfully describes many 1D FWM [23] and the recent $S_{\mathbf{I}}$ 2DCS [20] experiments. For clarity we focus on the HH spectral region. Using time-dependent perturbation theory and rotating wave approximation, we find that two terms contribute to the third-order optical response in the phase-matching direction $\mathbf{k}_1 + \mathbf{k}_2 - \mathbf{k}_3$. These are represented by the double-sided Feynman diagrams shown in the bottom of Fig. 1 (left), where e and f represent, respectively, HH exciton and two-exciton manifolds and g represents the ground state (top right of Fig. 1). The rules of these diagrams are given in Ref. [17].

In both pathways, during t_1 and t_2 the system is, respectively, in a single (ρ_{eg}) and a double (ρ_{fg}) quantum coherence. The two paths differ only in the third interval t_3 [ρ_{eg} for (i) and ρ_{fe} for (ii)]. Signatures of two-exciton couplings thus show up along t_3 and t_2 but not t_1. We therefore look at (t_3, t_2) correlation plots. We display the signal by a double Fourier transform with respect to t_3 and t_2 with the corresponding conjugate frequencies Ω_3 and Ω_2, holding t_1 fixed, i.e., $\mathbf{S}_{\mathbf{III}}(\Omega_3, \Omega_2, t_1)$. In diagrams (i) and (ii), f can be either redshifted (bound) $f = 2e - \Delta_b$, unshifted $f = 2e$, or blueshifted (scattering) $f = 2e + \Delta_s$ relative to twice the HH exciton energy, $2e$. Red (blue) energy shift corresponds to two correlated excitons with the opposite (same) spins. Energy shifts from dressed states are negligible in the present weak-field $\chi^{(3)}$ limit, and thus the HF (mean-field) contribution gives energy-unshifted two excitons.

From diagrams (i) and (ii), we can predict the key features of $\mathbf{S}_{\mathbf{III}}(\Omega_3, \Omega_2, t_1)$. During t_3 and t_2, diagram (i) has, respectively, eg and fg resonances (by reading across the two vertical lines of the diagram). The signals from (i) thus occur at $(\Omega_3, \Omega_2) = (\omega_{eg}, \omega_{fg})$, corresponding to the two resonances. Considering only bound two excitons, $f = 2e - \Delta_b$, we have $(\omega_{eg}, \omega_{fg}) = (e, 2e - \Delta_b)$. This position is represented by a solid square in the 2D spectra schematically sketched at the bottom of Fig. 1. Similarly we can sketch all other peak positions arising from diagrams (i) and (ii). Open circles represent unshifted two excitons and solid (open) symbols represent redshifted (blueshifted) two excitons.

We now examine the five peaks in Fig. 1. We note that the peaks resulting from (i), are spread only along Ω_2 and form a vertical pattern since it has eg resonances along Ω_3, while for (ii) the peaks are spread along both axes (diagonal pattern). Four properties make this signal particularly useful for resolving various two excitons and even the detailed structure of the two-exciton continuum. First, along t_2 there are only fg resonances, and thus the Ω_2 axis provides a clean projection for two excitons, without interference from eg resonances. Second, the two-exciton correlation energy can be obtained from a single peak. Δ_b is extracted from the solid square at $(e, 2e - \Delta_b)$ and Δ_s from the open square at $(e, 2e + \Delta_s)$. In TIFWM, in contrast, Δ_b is determined by subtracting the energies of two peaks. However, the HF peak (the circle) is not always clearly visible for certain pulse polarizations and laser detunings. Third, the squares from (i) for different f are generally much stronger than triangles from (ii). Thus it is sufficient to get the two-exciton energies from the well-resolved and strong (i) peaks (squares) along Ω_2 even when the triangles are not resolved. Fourth, both axes Ω_2 and Ω_3 involve two-exciton resonances. Along Ω_2, there are only fg resonances, while along Ω_3 there is both eg (i) and fe (ii). Spreading two-exciton resonances along both axes is critical for the high resolution. Along Ω_3 the two-exciton contribution [fe in (ii)] is weaker than the single-exciton one [eg in (i)] and thus may not be easily resolved. However, we show later that even this weak signature along Ω_3 is crucial for achieving high resolution when combined with the information from the Ω_2 projection.

Using the tight-binding Hamiltonian [22,23] with 10 sites, we have implemented the $\chi^{(3)}$ formalism for closing the infinite hierarchy of equations that has been widely applied to semiconductors [2,24]. In Fig. 2, we present the simulated 2D spectra obtained by solving Eqs. 20 and 21 of Ref. [19] using periodic boundary conditions. Using the same parameters of Ref. [25], we set the dephasing times for excitons $\tau_{\mathrm{ex}} = 2$ ps and two excitons $\tau_{2\mathrm{ex}} = 1$ ps in panels a–e. Panel e is obtained by cross-circular Gaussian pulses, where $\mathbf{k}_s$ is linearly polarized and $\mathbf{k}_3$, $\mathbf{k}_2$, and $\mathbf{k}_1$ are, respectively, right, left, and right circularly polarized. All other panels are calculated with colinear Gaussian pulses. Pulse parameters are chosen such that redshifted

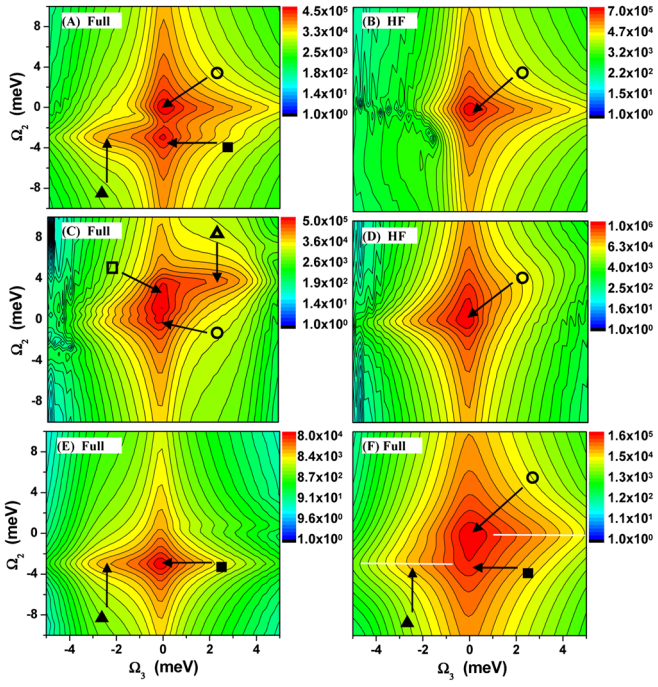

FIG. 2 (color online). Calculated $\mathbf{S}_{\mathbf{III}}(\Omega_3, \Omega_2, t_1)$ for (a) and (b), $\Delta_{\mathrm{opt}} = 3.9$ meV, $\omega_c = -2.85$ meV; (c) and (d), $\Delta_{\mathrm{opt}} = 1.8$ meV, $\omega_c = 2.15$ meV; (e), $\Delta_{\mathrm{opt}} = 3.9$ meV, $\omega_c = -3.85$ meV; and (f) $\Delta_{\mathrm{opt}} = 3.9$ meV, $\omega_c = -1.85$ meV.

two excitons are selectively excited. The optical power spectra width, Δ_{opt}, and carrier frequency, ω_c (relative to e) are given in the caption.

In all panels, the origin is e for Ω_3 and $2e$ for Ω_2. All peaks and shoulders are assigned using the symbols given in Fig. 1. Circles and solid squares are strong and well resolved along Ω_2, while solid squares and triangles are not resolved along Ω_3. The Ω_2 value of solid squares gives the TBE, Δ_b. Panels a and b are calculated, respectively, with and without correlated two excitons. As expected, features related to redshifted two excitons, such as the solid square and the triangle, disappear. Panels c and d repeat the calculations of panels a and b for pulses tuned to the blueshifted two excitons. One can obtain blueshifted TSE, Δ_s, from the open triangle (a shoulder but not a resolved peak) in panel c, even though we cannot resolve the open square from the two-exciton continuum. In panel e (cross-circular excitation), the HF contribution (the circle) at the origin $(e, 2e) = (0, 0)$ is absent. However, one can still obtain the TBE using the solid square. We also note that TBE may be extracted despite the large line broadening. Panel f shows the 2D spectrum calculated with faster dephasing times $\tau_{\text{ex}} = 1.0$ ps and $\tau_{2\text{ex}} = 0.5$ ps. Even though we can no longer resolve the circle and the solid square along the Ω_2 axis, it is still possible to obtain their energies from the "ridge" of the contour lines (two white lines). The TBE is given by the Ω_2 value of the bottom line.

The TBE can be obtained from the intense and well-resolved solid square in panel a. We thus circumvent the difficulty of probing TBE from the splitting between the solid square and the unresolved solid triangle, which overlap with eg and fe resonances along t_3. Additional calculations also show that the TBE-related solid square always has a solid triangle to the red, and the TSE-related open square always has an open triangle to the blue, as expected from Fig. 1. Moreover, the solid square and triangle (open square and triangle) always appear in pairs and we can easily obtain accurate TBE (TSE) by identifying both features, even when line broadening is large (e.g., panel f). The much weaker solid triangle from pathway (ii) plays a crucial role in identifying the solid square in panel f. Similarly, in panel c we cannot identify the open square without the help of the open triangle. Thus it is impossible to resolve the signature of blueshifted two excitons (unresolved open square and triangle) in panel c with conventional 1D FWM where the signature will either be covered by the two-exciton continuum along Ω_2 or along Ω_3 by the broadening of the much stronger single-exciton peak, the circle. This signature cannot be obtained from any other 2DCS techniques where two excitons show up along a single axis. However, with the panoramic 2D view offered by $\mathbf{S_{III}}$, we can easily obtain very accurate TSE, even though the open square and the triangle are weak and may not be resolved along any single axis.

In $\mathbf{S_I}$, we had demonstrated the first partial separation of two excitons [19] along Ω_3 due to the overlapping eg and fe resonances along t_3, as shown by the elongation of peaks in both experiments and simulations [19,20]. $\mathbf{S_{III}}$ provides an additional separation of two excitons by spreading them along Ω_2. Without this separation, one cannot resolve any two-exciton features in panel f, let alone the accurate TBE. It is the combination of the two dimensions Ω_3 and Ω_2 that makes it possible to go from the two ambiguous, unresolved open square and triangle in panel c to retrieve the unique signature of blueshifted two excitons and obtain the TSE.

The $\mathbf{S_{III}}$ technique provides a new perspective into the capacity of TIFWM experiments to provide TBE [9,10]. Let us recast the existing TIFWM signal using the present 2DCS terminology. The two-pulse signals [9] along $2\mathbf{k}_b - \mathbf{k}_a$ are given by $W_A(t_1) = \int_{-\infty}^{+\infty} |S_{\mathbf{I}}(t_3, t_2 = 0, t_1)|^2 dt_3$ (positive delay) and $W_B(t_2) = \int_{-\infty}^{+\infty} |S_{\mathbf{III}}(t_3, t_2, t_1 = 0)|^2 dt_3$ (negative delay). Three-pulse TIFWM signals [10] along $\mathbf{k}_a + \mathbf{k}_b - \mathbf{k}_c$ correspond to $W_C(t_2) = \int_{-\infty}^{+\infty} |S_{\mathbf{III}}(t_3, t_2, t_1 = t_1^0)|^2 dt_3$ (positive delay) and $W_D(t_2) = \int_{-\infty}^{+\infty} |S_{\mathbf{II}}(t_3, t_2, t_1 = t_1^0)|^2 dt_3$ (negative delay). Strong quantum beats show up only in W_B and W_C, both related to $S_{\mathbf{III}}$ and depend on t_2. This is clear from our pathway analysis. First, along t_2 there are only two-exciton resonances (fg) as shown in diagrams (i) and (ii) of Fig. 1, and thus we have well-defined quantum beats along t_2 and well-resolved peaks along Ω_2. Second, the squares from (i) show up mainly as eg resonances along t_3 and can be much stronger than the triangles, although they are all induced by correlated two excitons. Without such correlations, there will only be a circle at the origin. It is the stronger solid square and circle that give quantum beats. However, there are no appreciable beats for W_A and W_D. Figure 3 shows the pathways for $S_{\mathbf{I}}$ and the schematic 2D spectra pro-

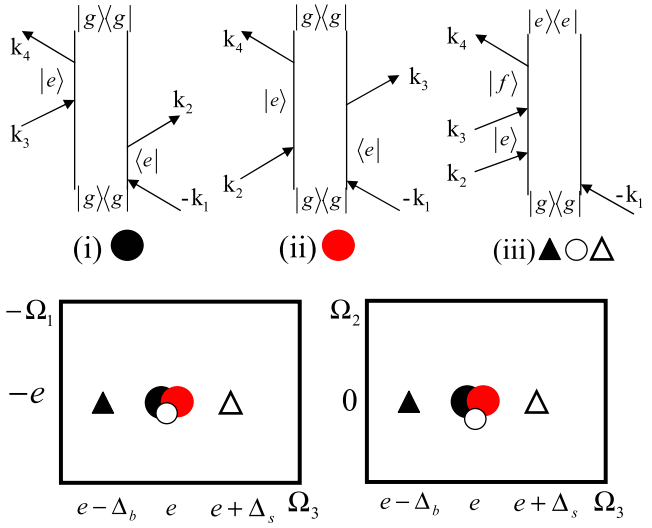

FIG. 3 (color online). Top: Feynman diagrams of the $S_{\mathbf{I}}$ technique. Bottom: Schematic 2D spectra, $S_{\mathbf{I}}(\Omega_3, t_2, -\Omega_1)$ (left) and $S_{\mathbf{I}}(\Omega_3, \Omega_2, t_1)$ (right).

jected, respectively, onto $(\Omega_3, -\Omega_1)$ and (Ω_3, Ω_2). Obviously, there is no two-exciton splitting along either Ω_1 or Ω_2 and thus $S_{\mathbf{I}}$ does not show quantum beats with respect to t_1 or t_2, as in W_A. A similar conclusion applies to $S_{\mathbf{II}}$, which corresponds to W_D. The only axis along which quantum beats occur for $S_{\mathbf{I}}$ and $S_{\mathbf{II}}$ is t_3. However, it is hard to observe such beats with any technique (including $S_{\mathbf{III}}$), because there are always dominant eg resonances along t_3 for all three 2DCS techniques, and thus the two-exciton resonances are not well resolved.

$\mathbf{S_{III}}$ also demonstrates an important limitation of TIFWM in probing TBE. Our calculations show that TIFWM yields the correct TBE only in ideal cases such as Fig. 2(a) where the Ω_2 coordinate of the circle coincides with $2e$ and its intensity is comparable to the solid square. However, the Ω_2 value and intensity of the circle are very sensitive to the pulse width, detunings, and pulse polarizations and are further affected by the cancellation of the two-exciton continuum to the HF portion. Calculations with long dephasing times (not shown) also suggest that the two-exciton continuum is far from uniform. Although the solid square has a fixed Ω_2, its intensity is also very sensitive to the pulse properties. Therefore the circle and the solid square do not always dominate the signal. Other components from the two-exciton continuum or even the open square may also contribute or even dominate the quantum beats. This makes the beating experiment less accurate for probing TBE. Furthermore, in the most favorable case for probing TBE where only bound two excitons are generated [e.g., the cross-circular excitations in Fig. 2(e)], the HF peak (circle) disappears completely. In this case, any beating frequency obtained is not connected to TBE. Therefore, one has to use other pulse polarizations to obtain quantum beats where the position and the intensity of the circle are affected by other types of two excitons.

In summary, the proposed 2DCS technique, $S_{\mathbf{III}}$, is intrinsically sensitive to two-exciton correlations and can distinguish between different species of excitons and two excitons in photoexcited semiconductors by spreading them along two axes. Combining the information from different Liouville-space pathways [17], $S_{\mathbf{III}}$ can accurately retrieve TBE even when it is smaller than exciton line broadening. We further report a clear signature of correlated unbound two excitons lying underneath the two-exciton continuum. $S_{\mathbf{III}}$ also provides new insights into the quantum beats in the most accurate TIFWM for obtaining TBE [9,10] of quantum wells, which are dominated by one of the two pathways and generally do not provide accurate TBE.

The support of the Chemical Sciences, Geosciences, and Biosciences Division, Office of Basic Energy Sciences, U.S. Department of Energy is gratefully acknowledged.

[1] H. Haug and S. W. Koch, *Quantum Theory of the Optical and Electronic Properties of Semiconductors* (World Scientific, Singapore, 2004), 4th ed.
[2] V. M. Axt and S. Mukamel, Rev. Mod. Phys. **70**, 145 (1998).
[3] F. Rossi and T. Kuhn, Rev. Mod. Phys. **74**, 895 (2002).
[4] Th. Östreich, K. Schönhammer, and L. J. Sham, Phys. Rev. B **58**, 12 920 (1998).
[5] W. Schäfer, D. S. Kim, J. Shah, T. C. Damen, J. E. Cunningham, K. W. Goossen, L. N. Pfeiffer, and K. Köhler, Phys. Rev. B **53**, 16 429 (1996).
[6] J. Shah, *Ultrafast Spectroscopy of Semiconductors and Semiconductor Nanostructures* (Springer, New York, 1999), 2nd enlarged ed.
[7] D. S. Chemla and J. Shah, Nature (London) **411**, 549 (2001).
[8] V. M. Axt and T. Kuhn, Rep. Prog. Phys. **67**, 433 (2004).
[9] H. Wang, J. Shah, T. C. Damen, and L. N. Pfeiffer, Solid State Commun. **91**, 869 (1994).
[10] E. J. Mayer, G. O. Smith, V. Heuckeroth, J. Kuhl, K. Bott, A. Schulze, T. Meier, D. Bennhardt, S. W. Koch, P. Thomas, R. Hey, and K. Ploog, Phys. Rev. B **50**, 14 730 (1994).
[11] M. Koch, J. Feldmann, G. von Plessen, E. O. Göbel, P. Thomas, and K. Köhler, Phys. Rev. Lett. **69**, 3631 (1992).
[12] S. T. Cundiff, M. Koch, W. H. Knox, J. Shah, and W. Stolz, Phys. Rev. Lett. **77**, 1107 (1996).
[13] R. R. Ernst, G. Bodenhausen, and A. Wokaun, *Principles of Nuclear Magnetic Resonance in One and Two Dimensions* (Clarendon, Oxford, U.K., 1987).
[14] S. Mukamel, Annu. Rev. Phys. Chem. **51**, 691 (2000).
[15] M. C. Asplund, M. T. Zanni, and R. M. Hochstrasser, Proc. Natl. Acad. Sci. U.S.A. **97**, 8219 (2000).
[16] T. Brixner, J. Stenger, H. M. Vaswani, M. Cho, R. E. Blankenship, and G. R. Fleming, Nature (London) **434**, 625 (2005).
[17] S. Mukamel, *Principles of Nonlinear Optical Spectroscopy* (Oxford University Press, New York, 1995).
[18] Xiaoqin Li, Tianhao Zhang, Camelia N. Borca, and Steven T. Cundiff, Phys. Rev. Lett. **96**, 057406 (2006).
[19] L. Yang, I. V. Schweigert, S. T. Cundiff, and S. Mukamel, Phys. Rev. B **75**, 125302 (2007).
[20] I. Kuznetsova, P. Thomas, T. Meier, T. Zhang, X. Li, R. P. Mirin, and S. T. Cundiff, Solid State Commun. **142**, 154 (2007).
[21] W. Langbein and B. Patton, J. Phys. Condens. Matter **19**, 295203 (2007).
[22] C. Sieh, T. Meier, F. Jahnke, A. Knorr, S. W. Koch, P. Brick, M. Hübner, C. Ell, J. Prineas, G. Khitrova, and H. M. Gibbs, Phys. Rev. Lett. **82**, 3112 (1999).
[23] T. Meier, P. Thomas, and S. W. Koch, *Coherent Semiconductor Optics: From Basic Concepts to Nanostructure Applications* (Springer, New York, 2006).
[24] V. M. Axt and A. Stahl, Z. Phys. B **93**, 195 (1994).
[25] S. Weiser, T. Meier, J. Möbius, A. Euteneuer, E. J. Mayer, W. Stolz, M. Hofmann, W. W. Rühle, P. Thomas, and S. W. Koch, Phys. Rev. B **61**, 13 088 (2000).